

# Millimeter-Wave Wideband High Efficiency Circular Airy OAM Multibeams with Multiplexing OAM Modes Based on Transmission Metasurfaces

Hui-Fen Huang\* and Hong-Ming Huang

**Abstract**—In this paper, wideband and high efficiency millimeter-wave circular Airy orbital angular momentum (OAM) beams, which have desired multiplexing OAM modes, directions, and beam numbers, are generated by the proposed three metal layer transmission metasurfaces (TMSs) with size  $12\lambda_0 \times 12\lambda_0$  based on the Airy-OAM phase superposition method. The measured results indicate non-diffracting propagation distance  $31\lambda_0$ , autofocusing property, high aperture efficiency 13.1%, and wideband 16.8% (28 GHz–33 GHz). The design method can be used for circular Airy OAM beam generation in point-to-point, point-to-multipoint wireless power transmission (WPT), and OAM mode multiplexing communication systems.

## 1. INTRODUCTION

In recent years, the application of vortex beams carrying OAM in large-capacity wireless communications [1], imaging [2], and other fields has received extensive attention. However, the divergence angle of the vortex beam expands with the increase in OAM mode number [3]. Recently, circular Airy beam has attracted great interests because of its non-diffracting, self bending, and abrupt autofocusing characteristics. The circular Airy beams gradually become Bessel beams in the far-field after they propagate a certain distance [4]. The autofocusing point and focal length can be controlled by appropriately selecting related parameters [5]. For many applications it is crucial that a beam abruptly focuses its energy right before a target while maintaining a low intensity profile until that very moment, such as medical treatment [6], generation of a light bullet [7], microparticle manipulation [8], security communications, WPT, high data rate, and efficiency communication systems [9]. In general, above involve the estimation of the capacity for the case of a wireless communication system operating in a fading environment [10]. In this paper, the non-diffracting and autofocusing characteristics of the circular Airy beam are used to alleviate the vortex beam-divergence problem.

Airy quantum wave packets of infinite extent were first discovered by Berry and Balazs from the Schrödinger equation in 1979 [11]. However, Airy waves were initially considered physically unrealizable with finite aperture due to the infinite energy content. In 2007, Siviloglou and Christodoulides introduced an extra exponential decaying factor and experimentally observed finite energy Airy beam optical field [12]. Since then, Airy beams have been widely investigated in optics [4–8] and in terahertz (THz) domain [13–15]. Researchers also found tremendous applications for mm-wave and microwave Airy beams. However, the experimental realizations for optics and THz cannot be used in microwave and mm-wave because huge size devices are required. Several theoretical analysis and numerical investigations are made in the microwave and millimeter-wave (mm-wave) bands [16]. Researchers

---

*Received 24 February 2022, Accepted 14 April 2022, Scheduled 26 April 2022*

\* Corresponding author: Hui-Fen Huang (huanghf@scut.edu.cn).

The authors are with the School of Electronic and Information Engineering, South China University of Technology, Guangzhou, China.

have tried to experimentally generate microwave and mm-wave Airy beams by employing metasurface and microstrip patches [17]. A new Airy family — radially symmetric/circular Airy beams are originally reported by Efremidis and Christodoulides in 2010 [4], and have been studied intensively due to their autofocusing property. Many research results have been obtained at optical frequencies including practical application potentials and controlling the beams, such as intensity contrast, locations, and focal pattern of the focal point [18]. Ring-Airy beams in THz waves have 5.3 times the pulse energy of the standard Gaussian THz waves, which have potential applications for the remote sensing of chemical, biological, and explosive materials from a standoff distance [19]. Autofocusing circular Airy beam has great application potential in mm wave and microwave for long-distance high-efficiency WPT and security communication.

The above proposed methods are mainly focused on generating Airy beams without OAM vortex. A 2-D Airy OAM beam is generated in [20]. Recently, circular Airy OAM beams with autofocusing property in mm-wave frequency band are reported [9, 21]. However, there are not many research results for circular Airy OAM beams, and the published Airy OAM beams carry single beam along  $z$  axis with single OAM mode.

In this paper, mm-wave circular Airy OAM beams, which have desired multiplexing OAM modes, directions, and beam numbers, are generated by TMSs. The developed TMSs have the advantages of wideband 16.4% and high aperture efficiency 13.1%. The paper is organized as follows. Section 2 is the unit design. TMS design and performance analysis are in Section 3. Experimental results are given in Section 4, and Section 5 is conclusion.

## 2. UNIT DESIGN

### 2.1. Phase Shift Compensation Principle

The schematic diagram for the proposed circular Airy OAM antenna is shown in Fig. 1. It consists of two parts: a horn feeder (with 3 dB beamwidth  $27.2^\circ$ ) and TMS, which can produce additional phase-shift  $\Delta\varphi$  to the incident wave by organizing the  $(i, j)$ th unit on the TMS. The coordinate origin is in the center of the TMS, and the horn is located at  $(0, 0, 35\text{ mm})$ . Then, the spherical wave from the horn feeder is converted into a high-gain circular Airy OAM beam by the TMS. The simulation is done by the CST Microsoft Studio, and the operation center frequency is 30 GHz.

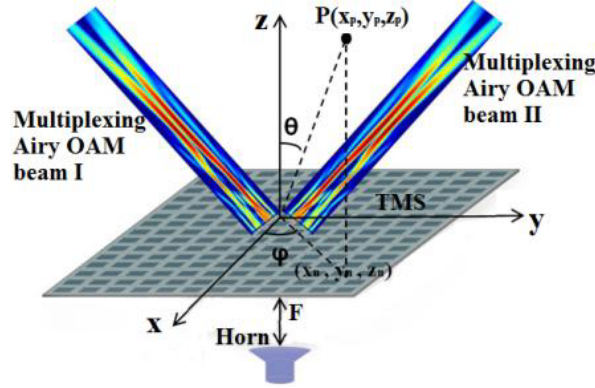


**Figure 1.** Schematic diagram of the proposed TMS for multiplexing Airy OAM beams.

In order to obtain spiral phase wavefront for  $n$  independent OAM beams with mode  $l_m$ , the required compensated phase shift  $\Delta\varphi$  for the  $(i, j)$ th unit is as follows [22]:

$$\Delta\varphi_{1(i,j)} = \frac{2\pi}{\lambda_0} K_{i,j} + \arg \left\{ \sum_{\vec{u}_m} \exp \left[ j \cdot \left( \frac{2\pi}{\lambda} \vec{r}_{i,j} \cdot \vec{u}_m + l_m \times \tan^{-1} \left( \frac{y_j}{x_i} \right) \right) \right] \right\} \quad (1)$$

where  $\vec{u}_m = (\sin \theta_m \cos \varphi_m, \sin \theta_m \sin \varphi_m, \cos \theta_m)$  is the  $m$ th beam direction;  $m$  is in the range of  $1 \sim n$ ;  $\lambda_0$  is the free space wavelength;  $r_{(i,j)}$  is the distance from the  $(i, j)$ th unit to the coordinate origin;

and  $K_{(i,j)}$  is the distance between the phase center of the feed and the  $(i, j)$ th unit at the position  $(x_i, y_j)$ . In order to generate  $n$  independent Airy beams, the following additional phase shift should be compensated [21].

$$\Delta\varphi_{2(i,j)} = \arg \sum_{m=1}^n \{Ai(b_0(r_{0(m)} - r_{(i,j)}))\} \quad (2)$$

where  $Ai(\cdot)$  is the Airy function,  $r_{0(m)}$  the main ring radius of the  $m$ th circular Airy beam, and  $b_0$  a constant. The initial radius of the circular Airy beam is approximately equal to  $(r_0 + 1/b_0)$ . The radius of the circular Airy beam decreases as it propagates and abruptly autofocuses at the focal point  $z_f$ , i.e., the beam radius essentially becomes zero at  $z = z_f$ . This shrinkage in radius from  $(r_0 + 1/b_0)$  to 0 is equivalent to a deviation of [4]

$$D = r_0 + 1/b_0 \quad (3)$$

where  $D = b_0^3 z_f^2 / 4k^2$ . The constant  $b_0$  is obtained by setting the desired  $z_f$  and  $r_0$  in Eq. (4). Here  $r_0$  and  $z_f$  are assumed to be  $0.1D$  and  $240$  mm, respectively, and the optimized  $b_0$  is  $1.25r_0$ . Then, the total compensation phase  $\Delta\varphi(x_i, y_j)$  for each unit to generate  $n$  Airy OAM beams is in Eq. (4):

$$\Delta\varphi(x_i, y_j) = \Delta\varphi_{1(i,j)} + \Delta\varphi_{2(i,j)} \quad (4)$$

### 2.2. Unit Analysis

The unit in Fig. 2 is used to cover  $360^\circ$  phase shift to produce a desired circular Airy OAM beam at 30 GHz. The unit consists of three metal layers separated by an F4B substrate with dielectric constant 2.2 and thickness 3 mm. Two mutually orthogonal narrow rectangular stripes are in the top and bottom layers, respectively, and the middle layer is a evolved split ring. Figs. 2(a)–(d) are the simulated Floquet ports model, front views of three metal layers at the top, middle, and bottom layers, respectively. The top and bottom metal layers act as  $x$ - and  $y$ -polarization selections, respectively, and the middle layer is responsible for polarization conversion and phase shift adjusting. The geometry parameters marked in Fig. 2 are as follows:  $p = 4$  mm,  $h = 0.5$  mm,  $a = 1.25$  mm,  $d = 0.3$  mm,  $w = 0.3$  mm,  $s1 = s2 = 0.75$  mm,  $g1 = 0.25$  mm,  $g2 = 0.5$  mm. The phase shift is controlled by adjusting the geometry parameters  $L$  and the rotation angle  $\varphi$  of the evolved split ring.

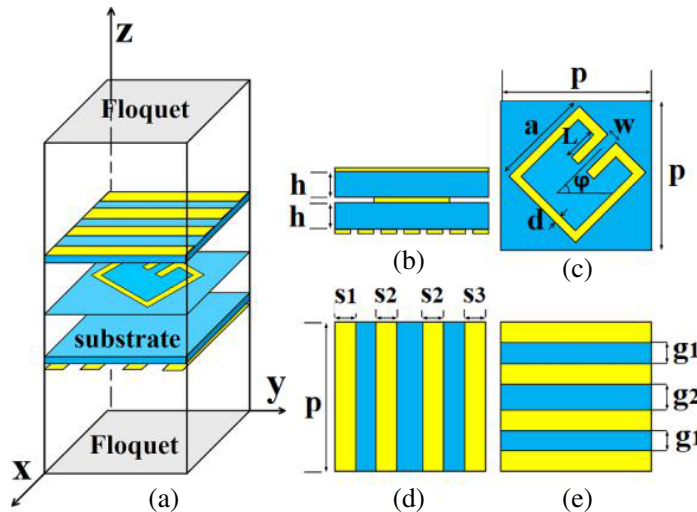


**Figure 2.** The proposed unit structure. (a) 3D schematic view. (b) Side view. (c) Middle metal layer. (d) Top metal layer. (e) Bottom metal layer.

The two mutually orthogonal narrow rectangular stripe arrays in the top and bottom layers form a Fabry-Pérot-like cavity. The unit has high efficiency polarization-conversion efficiency because the Fabry-Perot resonance enhances the polarization-conversion, and the consequent interference of

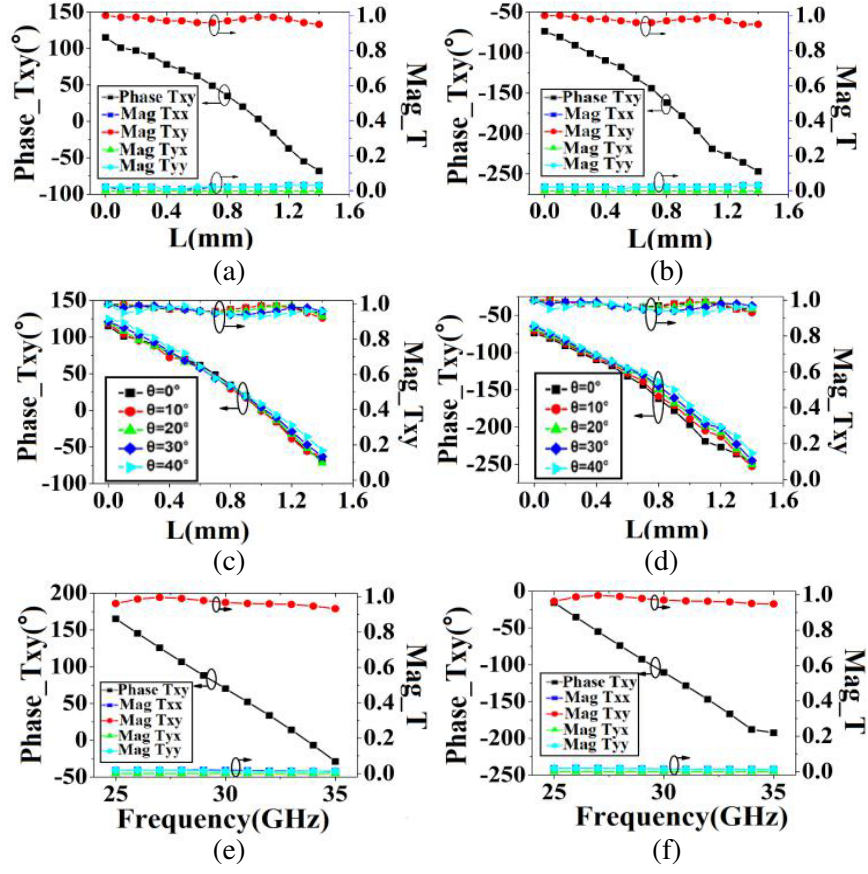


**Figure 3.** Phase shift/transmission coefficient  $T$  curves vs geometry parameter  $L$ : (a) for  $\varphi = 45^\circ$ , (b) for  $\varphi = -45^\circ$ , (c) for different incident angles and  $\varphi(45^\circ)$ , (d) for different incident angles and  $\varphi(-45^\circ)$ . Phase shift/transmission coefficient  $T$  curves vs frequency: (e) for  $\varphi = 45^\circ$  and  $L = 0.5$  mm, (f) for  $\varphi = -45^\circ$  and  $L = 0.5$  mm.

polarization couplings in the multireflection process may reduce the overall reflected fields with co- and cross-polarizations [23]. The interlayer coupling among the three metal layers is crucial to the broadband polarization transformation functionality [24]. We validated this concept by performing fullwave numerical simulations. Figs. 3(a), (b) are the simulated phase shift/transmission coefficient  $T$  vs the geometry parameter  $L$  curves for  $\varphi(45^\circ)$  and  $\varphi(-45^\circ)$ , respectively.  $L$  is increased from 0 mm to 1.4 mm. First, transmission coefficient  $T$  is analyzed. When the  $y$ -polarized EM waves incident on the bottom layer propagate along the  $z$  direction,  $T_{xy}$  remains above 0.95, and  $T_{yy}$  is close to zero, where  $T_{xy}$  and  $T_{yy}$  represent the transmission coefficient of the cross-polarized and co-polarized waves. Zero co-polarized and high efficiency cross-polarization transmission occurs. When the  $x$ -polarized waves is normally incident on the bottom layer along the  $z$  direction, both  $T_{xx}$  and  $T_{yx}$  keep near zero. It indicates that the  $x$ -polarized waves cannot pass through the bottom layer. The same is for  $x$ -/ $y$ -polarized waves incident on the top layer along  $-z$  direction. The phase shift is from  $-68^\circ$  to  $115^\circ$  for  $\varphi(45^\circ)$  as in Fig. 3(a), and from  $-247^\circ$  to  $-75^\circ$  as in Fig. 3(b), and then the phase shift covering  $362^\circ$  is obtained. Figs. 3(c), (d) are the simulated phase shift/transmission coefficient  $T$  vs the geometry parameter  $L$  curves in different oblique incident angles ( $\theta$ ) for  $\varphi(45^\circ)$  and  $\varphi(-45^\circ)$ , respectively. There is no obvious mismatch for the phase shift/ $T$  curves below  $40^\circ$  oblique incidence angle. Figs. 3(e), (f) depict the simulated phaseshift/transmission coefficient  $T$  as a function of frequency when  $L = 0.5$  mm. When the  $y$ -polarized EM waves are normally incident on the bottom layer along the  $z$  direction, we can clearly see that  $T_{xy}$  keeps higher than 0.95 within a wide frequency range  $28 \sim 33$  GHz. Meanwhile,  $T_{xx}$ ,  $T_{yx}$ , and  $T_{yy}$  keep a small value approximately equal to zero.

### 3. MS DESIGN AND PERFORMANCE ANALYSIS

#### 3.1. MS Design

$30 \times 30$  units form the circular Airy OAM transmitarray with size  $12\lambda_0 \times 12\lambda_0$  ( $\lambda_0$  at center frequency 30 GHz), and the unit period is 4 mm. The ratio of the aperture size to  $Z_f$  is 1. As an example, two kinds of Airy OAM transmitarrays with multiplexing OAM modes (+1 and +2) are designed: (1) Single beam. Two MS examples with beam directions of  $(\theta = 0, \varphi = 0)$  and  $(\theta = 60^\circ, \varphi = 0)$ , respectively. (2) Dual beams. One MS example with beams in the directions of  $(\theta_1 = 60^\circ, \varphi_1 = 0)$  and  $(\theta_2 = -60^\circ, \varphi_2 = 0)$ .

#### 3.2. Single Beam

Two Airy OAM MS examples have been designed with beam directions of  $(\theta_1 = 0, \varphi_1 = 0)$  and  $(\theta_2 = 60^\circ, \varphi_2 = 0)$ , respectively. The phase distributions for the two MS examples are calculated by the MATLAB program according to Eq. (4), and shown in Fig. 4(a). Then the corresponding geometry parameter  $L$  is determined according to Fig. 3. The near fields at 30 GHz have been simulated to verify the vortex and circular Airy properties. The simulated phase (in the focusing plane) and electric field (in  $xoz$  plane) distributions are in Figs. 4(b), (c), respectively. The spiral phase distributions indicate that the OAM modes are successfully generated. The beams have non-diffracting characteristics within a certain propagation distance near the Airy foci. The  $-3$  dB non-diffraction propagation distance ( $Z_{NDPD}$ ) for the two examples is about 315 mm. The simulated beam directions are  $(\theta_1 = 0, \varphi_1 = 0)$  and  $(\theta_2 = 58.6^\circ, \varphi_2 = 0)$ , which is basically consistent with the designed direction. The OAM-mode-spectrum distributions in the  $xoy$  plane at  $z = z_f$  are in Fig. 4(d), which reveal that the dominant OAM modes of  $l = 1$  and  $l = 2$  can be well distinguished, and they are bigger than the other crosstalk OAM modes by about 16 dB.

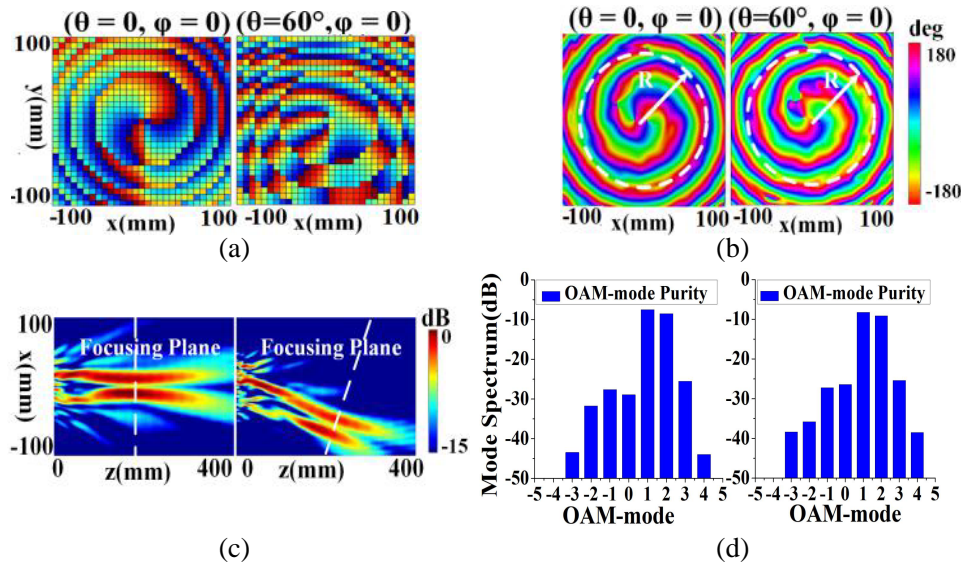


**Figure 4.** Simulated results for different single beams: (a) Compensated phase distribution. (b) Phase distribution in the focusing plane. (c) Electric field distribution on the  $xoz$  plane. (d) OAM mode purity in the focusing plane.

For OAM beam ( $l = 1, 2, \theta = 0, \varphi = 0$ ), a simulated near-field comparison between the Airy OAM beam and conventional (Conv.) OAM beam in  $xoz$  and  $xoy$  planes at 30 GHz is shown in Fig. 5. There is a certain non-diffracting propagation distance near the Airy focus for the Airy OAM beam as in Fig. 5(a). Three observing planes are taken at different distances to analyze the  $E$  field characteristics of the Airy OAM beam, as shown in Fig. 5(b). There are a maximum amplitude and a minimum size

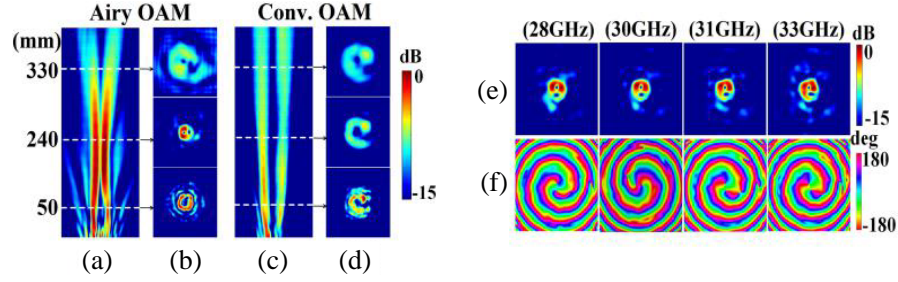


**Figure 5.** The  $E$ -field distributions. For the Airy OAM beam: (a) in the  $yo$  $z$  plane, and (b) in  $xoy$  plane on three observing plane. For the conventional OAM beam: (c) in the  $xoz$  plane, and (d) in  $xoy$  plane on three observing planes. The results for the Airy OAM beam in the focusing plane at  $z = 240$  mm at different frequencies: (e) amplitude, (f) phase.

of donut-shaped patterns at  $z = 240$  mm. Figs. 5(c), (d) show the  $E$ -field distributions of the Conv. OAM beam. The Airy OAM beam has convergence characteristics and smaller divergence angle than the Conv. OAM beam. The broadband property is proved by the  $E$ -field and phase distributions on the focal plane at  $z = 240$  mm at different frequencies as in Figs. 5(e), (f).

### 3.3. Dual Beam

The designed dual beams are  $(l = 1, 2, \theta_1 = 60^\circ, \varphi_1 = 0)$  and  $(l = 1, 2, \theta_2 = -60^\circ, \varphi_2 = 0)$ . Fig. 6(a) shows the electric field distribution in  $yo$  $z$ , and the  $-3$  dB non-diffraction propagation distance ( $Z_{NDPD}$ ) is about 310 mm. The simulated dual beam directions are  $(\theta_1 = 58.6^\circ, \varphi_1 = 0)$  and  $(\theta_2 = -58.5^\circ, \varphi_2 = 0)$ , which are consistent with the designed directions. Fig. 6(b) shows the electric field distributions for the dual beams in six  $xoy$  planes, that is, two focal planes, observation plane I/II/III and observation plane I'/II'/III' marked in Fig. 6(a). There are a maximum amplitude and a minimum size of donut-shaped patterns at  $z = 240$  mm, which can verify the autofocusing and non-diffraction properties in a propagation distance. The simulated phase and OAM-mode-spectrum distributions for the dual beams in the focal plane are shown in Fig. 6(c). The spiral phase distributions indicate that the OAM modes are successfully generated. Fig. 6(d) reveals that the dominant OAM modes of  $l = 1$  and  $l = 2$  can be well distinguished, and they are bigger than the other crosstalk OAM modes by about 13 dB.

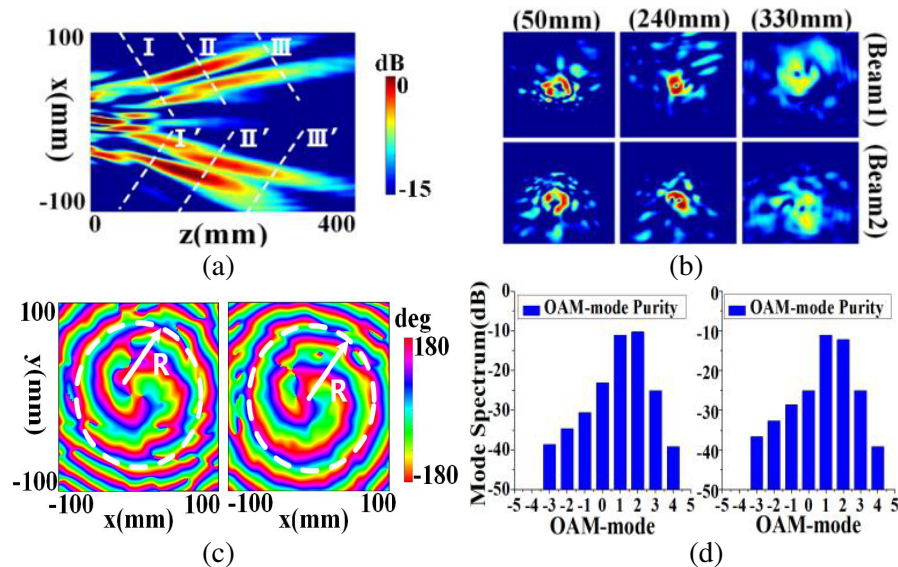


**Figure 6.** Simulated results for the dual beams. (a) Electric field intensity in the  $xoz$  plane. Results in the focusing planes: (b) electric field intensity, (c) phase OAM-mode-spectrum distributions.

### 4. MEASUREMENT RESULTS

In order to verify the design, a prototype was manufactured and tested for the MS with dual beams ( $l = 1, 2, \theta_1 = 60^\circ, \varphi_1 = 0$ ) and ( $l = 1, 2, \theta_2 = -60^\circ, \varphi_2 = 0$ ), which is shown in Fig. 7(a). Fig. 7(b) shows near field test environment. The feed uses a standard gain horn antenna, which is located at 50 mm of the MS.

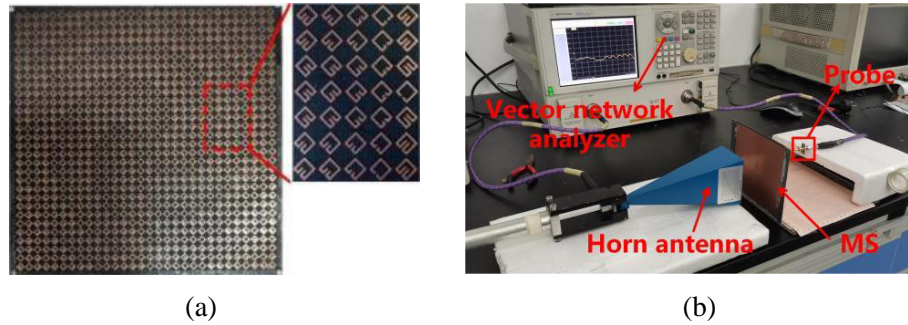


**Figure 7.** (a) The fabricated MS. (b) MS test environment.

Figure 8 shows the measured and simulated electric field intensity distributions at different frequencies on the  $xoz$  plane, and the simulated and measured results agree well. The maximum non-diffraction distance is about 304 mm. It is concluded that the dual Airy OAM beams carrying +1, +2 modes are generated from 28 to 33 GHz, and the OAM bandwidth is 16.4%. The measured aperture efficiency is 13.1% (The maximum gain of both beams is 14.7 dBi).

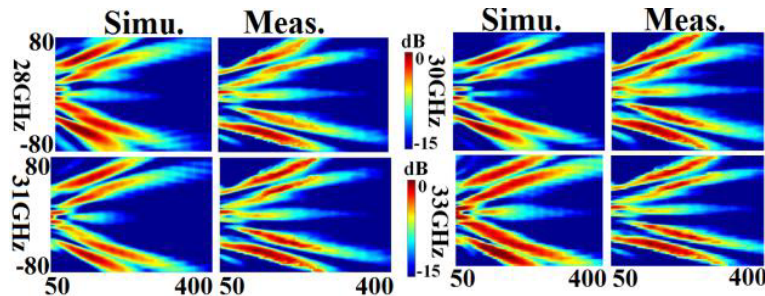


**Figure 8.** The simulated and measured electric field intensity on the  $yo z$  plane.

**Table 1.** Comparison between the proposed MS and the reported.

Ref.	$f_0$ (GHz)	Type	Non-diffracting beam	OAM mode	Aperture size $D(\lambda_0)$	$Z_{NDPD}(\lambda_0)$	$Z_{NDPD}/D$	Bandwidth	Aperture efficiency
[15]	400	Folded	Airy beam	no	53.3	26.7	0.5	Single frequency	Not mentioned
[25]	5.86	Transmitarray	Airy beam	no	22	78	3.55	1.4%	Not mentioned
[21]	47	Reflectarray	Airy beam	+1	70.5	391.7	5.56	10.8%	Not mentioned
[26]	10	Reflectarray	Bessel beam	+1 & +2	13.3	16.7	1.26	Single frequency	Not mentioned
<b>Our work</b>	<b>30</b>	<b>Transmitarray</b>	<b>Airy beam</b>	<b>+1 &amp; +2</b>	<b>12</b>	<b>31</b>	<b>2.63</b>	<b>16.4%</b>	<b>13.1%</b>

$\lambda_0$ : wavelength corresponding to the frequency  $f_0$ .

Table 1 shows the comparison between the proposed design and recent related studies. In the models proposed in [15, 25], the generated Airy beam does not have the OAM characteristics. Compared with the generation of Bessel vortex beams carrying multiple OAM modes [26], this work can generate Airy OAM beams with autofocusing and has larger  $Z_{\text{NDPD}}/D$  ratio. Compared with the nondiffractive Airy OAM single beam generated by reflectarray [21], we use transmission arrays, which have high aperture efficiency and high focusing efficiency, to generate multibeam with desired multiplexing OAM modes and beam directions. So the proposed circular Airy OAM TMSs have the advantages of multibeam, multiplexing OAM modes, wideband 16.4%, and high aperture efficiency 13.1%.

## 5. CONCLUSION

In this paper, TMSs with size  $12\lambda_0 \times 12\lambda_0$  are proposed to generate millimeter-wave circular Airy OAM beams with desired multiplexing OAM modes, directions, and beam numbers based on the Airy-OAM phase superposition method. The measured and simulated results agree well and validate the design method. The measured results indicate non-diffracting propagation distance  $31\lambda_0$ , autofocusing property, and high aperture efficiency 13.1%.

## ACKNOWLEDGMENT

This work was supported by the Key Project of Natural Science Foundation of Guangdong Province of China under Grant 2018B030311013, the National Natural Science Foundation of China under Grant 61071056.

## REFERENCES

1. Yan, Y., G. Xie, M. Lavery, et al., "High-capacity millimetre-wave communications with orbital angular momentum multiplexing," *Nat. Commun.*, Vol. 5, 4876, 2014.
2. Liu, K., Y. Cheng, X. Li, and Y. Jiang, "Passive OAM-based radar imaging with single-in-multiple-out mode," *IEEE Microwave and Wireless Components Letters*, Vol. 28, No. 9, 840–842, Sept. 2018.
3. Qin, F., L. Li, Y. Liu, W. Cheng, and H. Zhang, "A four-mode OAM antenna array with equal divergence angle," *IEEE Antennas and Wireless Propagation Letters*, Vol. 18, No. 9, 1941–1945, Sept. 2019.
4. Efremidis, N. K. and D. N. Christodoulides, "Abruptly autofocusing waves," *Optics Letters*, Vol. 35, No. 23, 4045–4047, Dec. 2010.
5. Hwang, C.-Y., K.-Y. Kim, and B. Lee, "Dynamic control of circular Airy beams with linear optical potentials," *IEEE Photonics Journal*, Vol. 4, No. 1, 174–181, Feb. 2012.
6. Mohanty, K., S. Mahajan, G. Pinton, M. Muller, and Y. Jing, "Observation of self-bending and focused ultrasound beams in the megahertz range," *IEEE Trans. Ultrason., Ferroelectr., Freq. Control*, Vol. 65, No. 8, 1460–1467, Aug. 2018.
7. Panagiotopoulos, P., D. Papazoglou, A. Couairon, and S. Tzortzakis, "Sharply autofocused ring-Airy beams transforming into non-linear intense light bullets," *Nature Commun.*, Vol. 4, No. 1, Oct. 2013, Art. no. 2622.
8. Zhang, P., J. Prakash, Z. Zhang, M. S. Mills, N. K. Efremidis, D. N. Christodoulides, and Z. Chen, "Trapping and guiding microparticles with morphing autofocusing Airy beams," *Optics Letters*, Vol. 36, No. 15, 2883–2885, 2011.
9. Kadlimatti, R. and P. V. Parimi, "Millimeter-wave nondiffracting circular Airy OAM beams," *IEEE Transactions on Antennas and Propagation*, Vol. 67, No. 1, 260–269, Jan. 2019.
10. Varzakas, P., "Optimal radio capacity for hybrid DS/SFH CDMA system in cellular radio," *IEE Electronics Letters*, Vol. 40, No. 7, 440–442, Apr. 2004.
11. Berry, M. V. and N. L. Balazs, "Nonspreading wave packets," *Amer. J. Phys.*, Vol. 47, No. 3, 264–267, 1979.

12. Siviloglou, G. A. and D. N. Christodoulides, "Accelerating finite energy Airy beams," *Optics Letters*, Vol. 32, No. 8, Apr. 15, 2007.
13. Niu, L., C. Liu, Q. Wu, K. Wang, Z. Yang, and J. Liu, "Generation of one-dimensional terahertz airy beam by three-dimensional printed cubic-phase plate," *IEEE Photonics Journal*, Vol. 9, No. 4, 1–7, Aug. 2017, Art no. 5900407, doi: 10.1109/JPHOT.2017.2712615.
14. Wang, T., et al., "Dual-band terahertz auto-focusing Airy beam based on single-layer geometric metasurfaces with independent complex amplitude modulation at each wavelength," *Adv. Theory Simul.*, Vol. 2, No. 7, Jul. 2019, Art. no. 1900071.
15. Miao, Z.-W., Z.-C. Hao, B.-B. Jin, and Z. N. Chen, "Low-profile 2-D THz Airy beam generator using the phase-only reflective metasurface," *IEEE Transactions on Antennas and Propagation*, Vol. 68, No. 3, 1503–1513, Mar. 2020.
16. Yang, Z., G. Wen, D. Insera, and Y. Huang, "Propagation range enhancement of truncated Airy beam with antenna array at microwave frequencies," *IEEE MTT-S Int. Microw. Symp. Dig.*, 1–3, May 2018.
17. Miao, Z.-W., Z.-C. Hao, and Q. Yuan, "Generation of one-dimensional Airy beams by a single-layer flexible metasurface at millimeter-wave band," *Proc. Asia-Pacific Microw. Conf. (APMC)*, 645–647, Nov. 2018.
18. Penciu, R.-S., K. G. Makris, and N. K. Efremidis, "Nonparaxial abruptly autofocusing beams," *Optics Letters*, Vol. 41, No. 5, 1042–1045, Mar. 2016.
19. Liu, K., A. D. Koulouklidis, D. G. Papazoglou, S. Tzortzakis, and X.-C. Zhang, "Enhanced terahertz wave emission from air-plasma tailored by abruptly autofocusing laser beams," *Optica*, Vol. 3, No. 6, 605–608, Jun. 2016.
20. Zhou, J., Y. Liu, Y. Ke, H. Luo, and S. Wen, "Generation of Airy vortex and Airy vector beams based on the modulation of dynamic and geometric phases," *Opt. Lett.*, Vol. 40, No. 13, 3193–3196, 2015.
21. Huang, Y., X. Li, Z. Akram, H. Zhu, and Z. Qi, "Generation of millimeter-wave nondiffracting Airy OAM beam using a single-layer hexagonal lattice reflectarray," *IEEE Antennas and Wireless Propagation Letters*, Vol. 20, No. 6, 1093–1097, Jun. 2021.
22. Yu, S. X., L. Li, G. Shi, et al., "Generating multiple orbital angular momentum vortex beams using metasurface in radio frequency domain," *Appl. Phys. Lett.*, Vol. 108, 2016.
23. Chiang, Y.-J. and T.-J. Yen, "A composite-metamaterial-based terahertzwave polarization rotator with an ultrathin thickness, an excellent conversion ratio, and enhanced transmission," *Appl. Phys. Lett.*, Vol. 102, 011129, 2013.
24. Wei, Z., Y. Cao, Y. Fan, et al., "Broadband polarization transformation via enhanced asymmetric transmission through arrays of twisted complementary split-ring resonators," *Appl. Phys. Lett.*, Vol. 99, 221907, 2011.
25. Huang, Y., et al., "Experimental demonstration of microwave two-dimensional Airy beam generation based on single-layer metasurface," *IEEE Transactions on Antennas and Propagation*, Vol. 68, No. 11, 7507–7516, Nov. 2020.
26. Feng, Q. and Y. Lin, "Generation and measurement of a bessel vortex beam carrying multiple orbital-angular-momentum modes through a reflective metasurface in the RF domain," *Phys. Rev. Applied*, Vol. 15, No. 8, 064044, Jun. 2021.